The Astronomical Journal, 137:5057–5067, 2009 June doi:10.1088/0004-6256/137/6/5057

OBSERVATIONS OF BINARY STARS WITH THE DIFFERENTIAL SPECKLE SURVEY INSTRUMENT. I. INSTRUMENT DESCRIPTION AND FIRST RESULTS

Elliott P. Horch[1,5,6], Daniel R. Veillette[2,5,7], Roberto Baena Gallé[3], Sagar C. Shah[2,5,8], Grant V. O'Rielly[2], and William F. van Altena[4]

[1] Department of Physics, Southern Connecticut State University, 501 Crescent Street, New Haven, CT 06515, USA; horche2@southernct.edu
[2] Department of Physics, University of Massachusetts Dartmouth, 285 Old Westport Road, North Dartmouth, MA 02747, USA; drv@usno.navy.mil, g_sshah@umassd.edu, gorielly@umassd.edu
[3] Departament d'Astronomia i Meteorologia, Universitat de Barcelona, Marti i Franquès 1, E-08028 Barcelona, Spain; rbaena@am.ub.es
[4] Department of Astronomy, Yale University P.O. Box 208101, New Haven, CT 06520, USA; william.vanaltena@yale.edu
Received 2009 January 26; accepted 2009 April 3; published 2009 May 6

ABSTRACT

First results of a new speckle imaging system, the Differential Speckle Survey Instrument, are reported. The instrument is designed to take speckle data in two filters simultaneously with two independent CCD imagers. This feature results in three advantages over other speckle cameras: (1) twice as many frames can be obtained in the same observation time which can increase the signal-to-noise ratio for astrometric measurements, (2) component colors can be derived from a single observation, and (3) the two colors give substantial leverage over atmospheric dispersion, allowing for subdiffraction-limited separations to be measured reliably. Fifty-four observations are reported from the first use of the instrument at the Wisconsin-Indiana-Yale-NOAO 3.5 m Telescope[9] in 2008 September, including seven components resolved for the first time. These observations are used to judge the basic capabilities of the instrument.

Key words: astrometry – binaries: close – binaries: visual – instrumentation: high angular resolution – instrumentation: interferometers – techniques: high angular resolution – techniques: interferometric – techniques: photometric

Online-only material: color figure

1. INTRODUCTION

Speckle imaging continues to provide the majority of astrometric data for subarcsecond-separation binary systems. This is largely due to the fact that it is an extremely efficient technique, easily permitting over 100 objects to be routinely observed per night by the most experienced speckle observers. In addition, there has been recent progress in understanding how to obtain reliable photometry from the method, through our own work (e.g., Horch et al. 2004, 2008) and the work of other investigators (Scardia et al. 2005, 2006, 2007; Balega et al. 2002, 2005, 2006; Tokovinin & Cantarutti 2008; Tamazian et al. 2008). This advance promises to be significant for our understanding of the stellar structure and evolution in the long term for the following reason. The standard stellar structure models require mass, helium abundance, metallicity, and age as the basic inputs. If well-determined magnitudes and colors can be obtained for many binaries in addition to individual masses (through orbit determinations) and system metallicity (through spectroscopic observations), the standard stellar evolution calculations become overdetermined. This is a strong position from which to investigate the details of stellar models, and one which is not possible without photometric information of the components of binary systems. Such information is also extremely important in the investigation of binaries with unusual components, as in the work of Tamazian et al. (2008) on the flare star CR Dra.

In order to take full advantage of this opportunity, we have developed a new speckle imaging system that takes data simultaneously in two colors. The instrument is known as the Differential Speckle Survey Instrument (DSSI). The basic design is similar to our previous instrument, the RIT-Yale Tip-tilt Speckle Imager (RYTSI), which is described in Meyer et al. (2006), in that a two-axis galvanometric scanning mirror system is used in combination with a large-format CCD imager to record a grid of speckle patterns over the entire chip prior to full-frame readout. In the case of the DSSI, a dichroic beamsplitter is placed after the mirror system in the optical path, which allows light above a cutoff wavelength to be sent to one CCD camera and light below that wavelength to be sent to a second CCD. Each CCD collects a sequence of speckle patterns where the observing conditions are identical, including the zenith angle. In that case, it becomes possible to distinguish between differential refraction and the presence of a companion below the diffraction limit, as discussed in Horch et al. (2006). This opens up a new separation range for binary star observations, providing more overlap with spectroscopic techniques and coming closer to what has been achieved with long baseline optical interferometry.

2. BASIC INSTRUMENT DESCRIPTION

The DSSI is very simple in design. A block diagram of the optical layout is shown in Figure 1. Focused light from the telescope is collimated by a short focal length lens at the front of the instrument. The collimated beam is then reflected off of the scanning mirrors that can combine to tip and tilt the beam, moving the image position in two orthogonal directions on the detector. (The galvanometer mirrors are referred to as the

[5] Visiting Astronomer, Kitt Peak National Observatory, National Optical Astronomy Observatory, which is operated by the Association of Universities for Research in Astronomy, Inc. (AURA) under cooperative agreement with the National Science Foundation.
[6] Adjunct Astronomer, Lowell Observatory.
[7] Current address: U.S. Naval Observatory, 3450 Massachusetts Ave. NW, Washington, DC 20392, USA.
[8] Current address: Science Department, Advanced Math and Science Academy Charter School, 201 Forest Street, Marlborough, MA 01752, USA.
[9] The WIYN Observatory is a joint facility of the University of Wisconsin-Madison, Indiana University, Yale University, and the National Optical Astronomy Observatories.

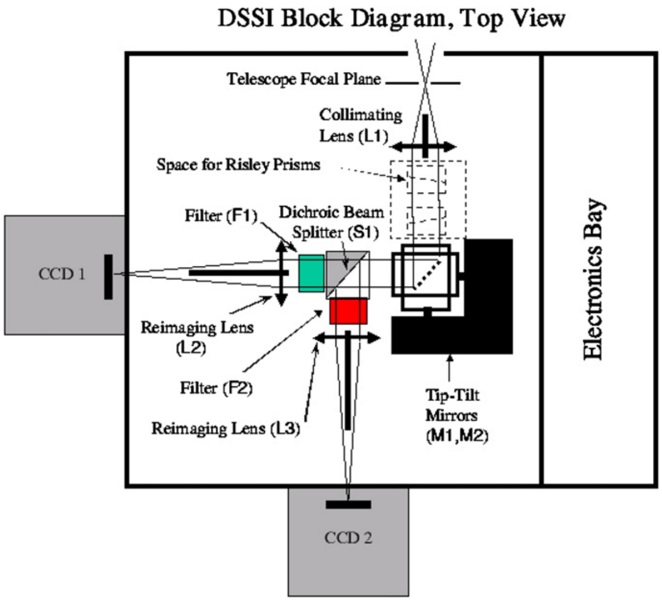

Figure 1. Basic components of the DSSI system.
(A color version of this figure is available in the online journal.)

tip-tilt system in Figure 1.) Between the collimating lens and the mirrors, there is space for the eventual inclusion of Risley prisms for high-dispersion compensation, if they prove to be needed at sites where the instrument is used. The Wisconsin-Indiana-Yale-NOAO (WIYN) Telescope has its own dispersion-correction optics on the Nasmyth port where we mounted the DSSI, and therefore this was not considered a high priority for including during the initial operation of the instrument. After reflecting off of the scanning mirrors, the beam passes through the dichroic beamsplitter. Mounted directly onto the beamsplitter housing on both the reflective and transmissive exit faces are narrow bandpass filters, appropriate for speckle observations. The two exit beams are focused with identical lenses that have focal lengths of roughly 7 times that of the collimating lens, so that a magnification of the same factor is achieved on the image plane. Light in both channels then comes to a focus on a Princeton Instruments PIXIS 2048B CCD camera. Both the collimating lens and the reimaging lens mounts are built to slide on tracks, similar to the RYTSI design. This permits different focal length lenses to be used (and therefore different magnifications to be obtained) depending on the focal ratio of the telescope.

The galvanometric scanning mirror system was purchased from Laserworks, Inc. of Orange, CA. The galvanometers are TS-3005PDs, driven by SA-525 amplifier boards, a combination that was chosen for its positional stability and high bandwidth. Each axis of the system is controlled by its own power supply, both of which are mounted in the electronics bay of the instrument. The driver boards for both mirrors are also located there. The analog input voltages needed to set the mirror positions and control the mirror motion are provided by a National Instruments multifunction PCI-6221 input/output board in the DSSI control computer. Software for the mirror control was written as a stand-alone program in Microsoft Visual C++. The aluminum housing for the instrument was custom-built by Anderson Tool Company of New Haven, CT.

All of the lenses, filters, and dichroics were obtained from Edmund Optics.[10] The elements available on the first run are shown in Table 1 and filter transmission curves obtained from manufacturer data are shown in Figure 2. The red–green dichroic was used for all observations and the transmissive port of the instrument was fitted with the 692 nm filter. On September 9, the reflective port of the dichroic was fitted with the 562 nm filter, and on September 10 and 11, the 447 nm filter was used. These filters were chosen so that their center wavelengths were close to those in the Johnson *UBVRI* system (specifically, the *B*, *V*, and *R* filters; see, e.g., Johnson 1965) and conversions onto that system will be manageable. We plan to add a near-infrared filter in the future where the center wavelength will be close to the *I* filter in the Johnson system as well, although *U*-band analogue is not envisioned due to the difficulties associated with obtaining high-quality speckle observations in the ultraviolet. While we will use a given filter pair for a whole night under normal circumstances, the dichroic and filter mount assembly is easily removed and replaced. We will have three such assemblies ready for future runs, each fitted with a different dichroic/filter combination.

Definitive filter transformation curves will be developed using future data from the instrument, but we have used the Pickles spectral library (Pickles 1998) and the filter transmission data provided by the manufacturer to obtain a first estimate of the difference between Johnson magnitudes and those obtained with the DSSI. Starting with the stellar flux, an instrumental magnitude was created for the desired DSSI filter by first computing the observed photon flux, which up to a constant multiplicative factor may be written as

$$f_{S,F} = \int_0^\infty [\lambda \cdot S(\lambda)] \cdot F(\lambda) \cdot D(\lambda) \cdot Q(\lambda) \cdot A(\lambda) d\lambda, \qquad (1)$$

where S is the stellar flux, F is the filter transmission, D is the dichroic transmission or reflection as appropriate, Q is the detector quantum efficiency, and A is the atmospheric transmission. The inclusion of λ in the first term of the integrand effectively converts from the flux to photon flux, and we assumed that the efficiency of the telescope and other DSSI optical elements was 1. The instrumental magnitude can then be formed using the standard formula

$$m_F = -2.5 \cdot \log(f_{S,F}) + C, \qquad (2)$$

where C is a constant. In order to compare with Johnson filters, we used the filter transmission curves for the *B*, *V*, and *R* filters available from the *General Catalogue of Photometric Data* Web site[11] (Mermilliod et al. 1997). When determining the magnitude in each Johnson filter, only the stellar flux and the filter transmission were included in the integrand of Equation (1). After choosing the constant for each filter so that an A0V star would have magnitude +0.65, we then determined magnitudes for a large range of luminosity class V spectral types (O5V to M5V). The appropriate flux ratio for each spectral type relative to the A0V flux was determined using absolute magnitude data from Schmidt-Kaler (1982). Figure 3 shows the comparison in magnitude between each DSSI filter and the corresponding standard filter as a function of the $B - V$ color. Given that most of the binaries that we observe have magnitude differences less than 5, we can conclude from the figure that the instrumental magnitude difference obtained in a DSSI filter will be no more than 0.1 mag different from the magnitude

[10] www.edmundoptics.com

[11] obswww.unige.ch/gcpd/gcpd.html

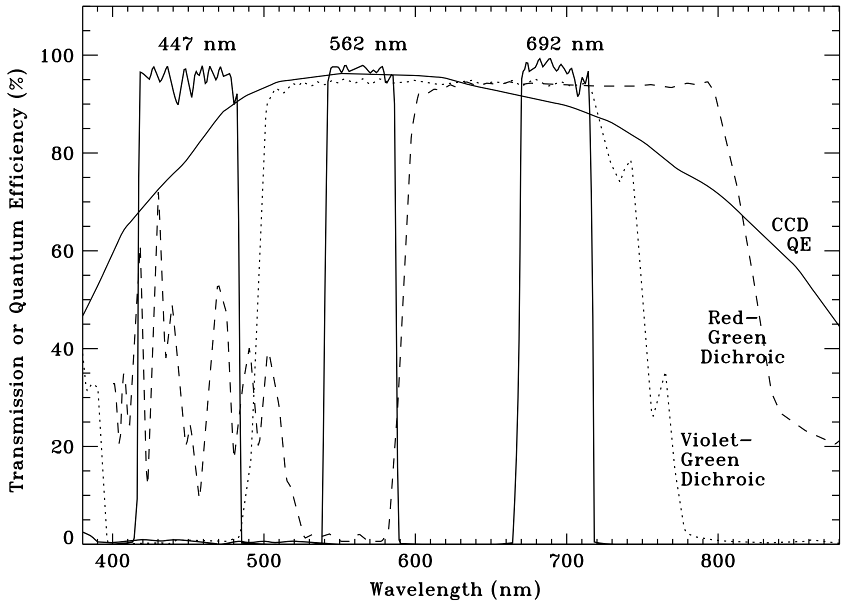

Figure 2. Transmission curves for the filters and dichroic elements in the DSSI. The CCD quantum efficiency curve is also overlaid. The data were obtained from the manufacturers.

Table 1
Optical Elements used in the DSSI

Element Type	Edmund Stock Number	Focal Length (mm)	λ (nm)	Δλ (nm)	Peak Transmission (%)	Peak Reflection (%)	Thickness (mm)
Blue Filter	NT48-074	···	447	60	97	···	3.5
Green Filter	NT48-085	···	562	40	97	···	5.0
Red Filter	NT48-148	···	692	40	99	···	3.5
Green-Red Dichroic	NT47-424	···	595	···	94	99	1.1
Violet-Green Dichroic	NT47-421	···	497	···	93	99	1.1
Collimating Lens	NT45-211	30	···	···	···	···	9.3*
Reimaging Lenses	NT45-179	200	···	···	···	···	9.1*

Note. * Edge thickness.

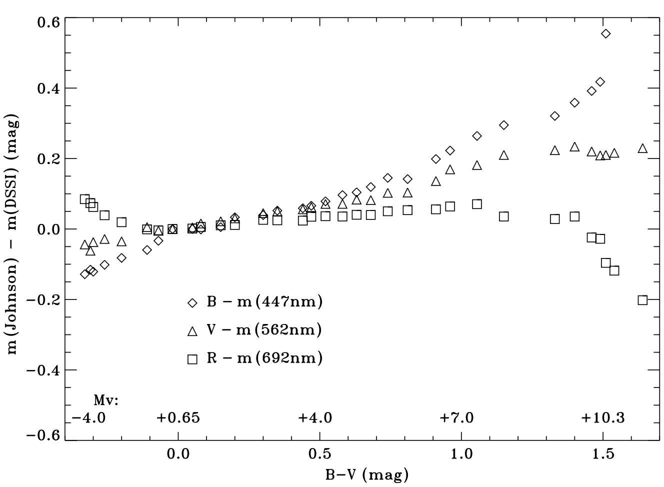

Figure 3. Magnitude differences between the Johnson system and the DSSI filters for luminosity class V stars as a function of $B - V$.

difference that would be obtained in the corresponding Johnson filter, except for very red systems.

The PIXIS CCD cameras have backthinned 2048×2048 pixel Marconi 42-40 arrays, with a peak quantum efficiency of 96%. The quantum efficiency is above 90% from approximately 480 to 700 nm. The cameras can be read out from either of two independent ports. The first reads a full frame in approximately 2 s with a read noise of 14–16 electrons, while the other reads the full frame in approximately 40 s with a read noise of 3–4 electrons. The latter was used exclusively on this run, though in the future we anticipate using the faster setting on brighter targets and reserving the slower setting for fainter objects. Software to control both cameras simultaneously was written in Microsoft Visual C++, using the software developer's toolkit provided by Princeton Instruments. Data files are written in the FITS format so that relevant observational parameters such as the observing time, sky position, and camera parameters can be stored in the data header. All program functions are displayed and controlled from a graphical user interface that allows point-and-click execution of commands, including the ability to read in observation lists so that the user can select objects to fill the data header with no typing.

3. OBSERVATIONS

The first observations with the instrument were obtained at the WIYN 3.5 m Telescope on 2008 September 9–11. Clouds, rain, and high humidity prevented the dome from being opened for about 70% of the time, so that the usable time amounted to approximately 10 hr over the three nights, the majority of which was on the 9th. Nonetheless, when conditions permitted us to observe, the seeing was sub-arcsecond, and we were able

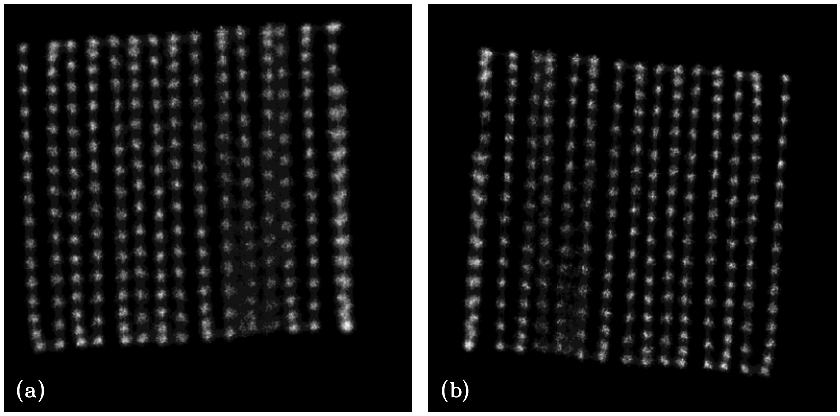

Figure 4. Raw data frames of HDS 423 = HIP 15737. (a) 562 nm. (b) 692 nm.

to obtain enough data to investigate the performance of the instrument as well as to calibrate the astrometric reductions.

Figure 4 shows two raw data frames taken simultaneously with the instrument. The slight tilt of the speckle patterns relative to the detector axes is due to a slight bend in the spindle of one of the galvanometers. We believe that we can correct this problem before any subsequent use of the system. Also note that the frames are essentially mirror images of one another, since there is an extra reflection in one of the two channels of the optical path because of the dichroic.

The plate scale and orientation angle for the observations were measured using exactly the same methods as described in Horch et al. (2008). Specifically, the plate scale was measured using a slit mask attached to the tertiary mirror baffle support structure. The telescope was then pointed at a bright unresolved star chosen from *The Bright Star Catalogue* (Hoffleit & Jaschek 1982). The presence of the slit mask produces fringes in the speckle patterns obtained, where the absolute scale of the fringes can be determined from the slit spacing, focal length, distance of the mask from the image plane, and the effective center wavelength of the observation. The first three quantities have been measured either by us or by WIYN personnel in the past, and these values were assumed. For the effective center wavelength, our practice has been to use the filter transmission curves, CCD quantum efficiency curve, atmospheric transmission curve available for Kitt Peak, and a stellar flux curve from the Pickles spectral library (Pickles 1998) that matches the object observed with the mask in order to model the correct wavelength. In the case of the DSSI data described below, the dichroic transmission/reflection curve was also incorporated into the model calculation. For the optical elements used in Table 1, the transmission curves shown in Figure 2 were assumed to be correct and were not independently measured. Our final values for the pixel scale are 16.958 ± 0.011 mas pixel^{-1} for the reflective channel and 18.03 ± 0.011 mas pixel^{-1} for the transmissive channel.

The orientation angle was determined by taking a series of 1 s exposures with the galvanometer mirrors in a fixed position, offsetting the telescope in different directions between exposures. This was done without autoguiding, so that there was some drift of the star position on the frame. Our standard sequence of offsets has redundancy of the starting position built in, so that over the sequence, the drift rate can be estimated and removed. For the orientation angle of the detector axes relative to sky coordinates, we obtained $-1.8 \pm 1^{\circ}\!.0$ for the reflective channel and $+3.6 \pm 1^{\circ}\!.1$ for the transmissive channel. The offset images also give values for the scale calibration, though they are of lower precision than the slit mask data. Nonetheless, the scale results from offset images were consistent with those of the mask to within the estimated uncertainty for both channels.

When analyzing the calibration data, it became clear that the scale in both channels of the instrument had a small dependence on the position angle relative to celestial north. The signature observed is consistent with a slight tilt to the image plane relative to the plane defined by each CCD array. It is probable that this is due to the galvanometer spindle problem mentioned above. The astrometric results discussed below were corrected for this effect by modeling the situation as a simple geometrical projection that was aligned with the celestial coordinate axes, so that a term proportional to $\sin^2\theta$ is introduced into the scale determination (where θ is the position angle). That is, the scale as a function of the position angle was approximated by

$$s(\theta) = s_0 \cdot [1 - \alpha \sin^2\theta], \tag{3}$$

where s_0 is the scale at $\theta = 0$ and α is a constant that determines the amplitude of the effect. In this case, a circular object would be mapped to an ellipse (of very low eccentricity) on the CCD. The 1 s orientation images discussed above were then evaluated to determine the major and minor axes of such a hypothetical ellipse on the CCD, as they represent offsets of an equal size in orthogonal directions. This yields the two orthogonal scale values (or, equivalently, the tilt angle of the image relative to the detector plane), which in turn determines the constant α above. We then tied this to the more precise mask data by requiring that the scale value exactly match that of the mask for the position angle at which the mask data were taken.

The observing routine consisted of identifying small groups of targets within a few degrees of one another on the sky and sequentially observing these objects before moving on to a different sky position. Observations were generally taken with hour angles of less than 1. In each grouping, we also observed a bright unresolved star from *The Bright Star Catalogue,* which could then serve as a point source calibration object in our reduction scheme. In all observations, the mirrors were set so that individual speckle images had an effective integration time of 50 ms.

4. RESULTS

Our method for analyzing CCD speckle data has been well documented in earlier papers, most recently in Horch et al. (2008). The same procedure was used for DSSI data, although each DSSI observation yields two data files instead of only one. Speckle images are extracted from the large CCD frames and an estimate of the bias level of the chip during the observation is made. As noted in Tyler et al. (2007), having good information about the CCD bias level is important for obtaining the best possible photometric information with CCD-based speckle observations. This bias level can be extracted from a region without signal information in each image being analyzed. In order to build a stack of speckles from the original CCD frame, a four-step algorithm is performed (Meyer et al. 2006). First, a smooth copy of the CCD frame is computed using a spatial filter that preserves the main shape of the star images. Second, a mask is created by thresholding the frame with a certain value, which creates disconnected regions of a uniform value where the speckle patterns are located. In the third step, the midpoint of each speckle pattern is calculated and is considered to be the center of a 128×128 pixel image where the speckle pattern is stored. Lastly, a stack of $N \times 128 \times 128$ images with all extracted speckle patterns is made, where N is the number of individual speckle images found. For observations on September 9, $N \sim 500$, and for September 10 and 11, $N \sim 1000$.

Once the bias-subtracted speckle images are prepared, the autocorrelation and triple correlation functions are computed, as is the standard practice in speckle imaging; see, e.g., Lohmann et al. (1983). We follow the practice of computing the so-called near-axissubplanes of the bispectrum, and using these to produce a diffraction-limited image of the target in combination with the object power spectrum. The reconstructed images are then used to determine the rough position of the secondary component. Once we have decided our preliminary positions, and associate with each system a suitable point source for the purpose of deconvolution, we determine the separation, position angle, and magnitude difference for each of the observations by performing a weighted least-squares fit to the spatial frequency power spectrum of the object with a cosine-squared function. In order to improve this fitting, we checked the consistency of the position angle and separation in both colors. For the data described below however, the separations and position angles were then averaged to obtain final astrometric results, while the magnitude differences obtained in each filter were not combined.

Table 2 shows our main table of results. The column headings give (1) the Washington Double Star Catalog number, which also gives the right ascension and declination of the object in J2000.0 coordinates; (2) *The Bright Star Catalogue* (HR), Aitken Double Star (ADS), Bonner Durchmusterung (BD) number, or Henry Draper (HD) number; (3) the discoverer designation; (4) the *Hipparcos* Catalogue number; (5) the Besselian Year of the observation; (6) the position angle, θ, in degrees, with North through East defining the positive sense of θ; (7) the separation, ρ, in arcseconds; and (8)–(10) the magnitude difference observed in each of the three filters listed in Table 1. The position angles have not been precessed, and so are appropriate for the epoch shown. The position angles and separations shown are the average of the results obtained in both filters in all cases where two magnitude differences are shown. If only one magnitude difference is shown for an observation, it is because the secondary was not clearly detected in the bluer filter used. (This is usually due to a large magnitude difference.) Seven of the entries in Table 2 have not been resolved before. We propose names of Yale-Southern Connecticut (YSC) 18 through 24 for these objects, following the group of objects resolved in Horch et al. (2008; YSC 1–17).

Figure 5 shows two examples of reconstructed images obtained from the data. In the first case, A 1910AB, the system does not have a large color difference between the components, so that the images from the two channels appear very similar, although the secondary is slightly brighter in the 562 nm frame. The spectral type appearing in the *Hipparcos* Catalogue (ESA 1997) is A0. On the other hand, the second object shown, HEI 35, which has spectral type K5, has a more noticeable difference in the height of the secondary peak between the two channels, in the sense that the redder filter gives a smaller magnitude difference. These images also give a rough measure of the quality that can be expected from the instrument as a function of the system magnitude; A 1910AB has a V magnitude of 6.8 while the V magnitude of HEI 35 is 9.1. In both cases, the images represent the result of approximately 30 s of data on each target.

4.1. *Astrometric Precision*

Although we have relatively few measures so far, we nonetheless attempt to roughly characterize the accuracy and precision of our astrometric measures with two methods. The first is to examine the differences between the position angles and separations between the two channels of the same observation. These are shown in Figure 6. The average difference in the position angle between the channels is $0.6 \pm 1^\circ\!.5$ while the average difference in separation is 0.55 ± 0.45 mas. The uncertainties in these numbers include those of the offset angle and scale determinations for each channel, and are dominated in the case of the position angle by the offset angle uncertainty. The standard deviations are $1.64 \pm 0^\circ\!.19$ and 2.71 ± 0.32 mas, respectively.

These numbers give the first estimate of the precision possible with the instrument and are independent of the scale and offset angle determinations. Assuming that the errors are Gaussian in nature, subtracting sets of two independent measures of the same intrinsic precision and no systematic error would result in a distribution with zero mean and a standard deviation of $\sqrt{2}$ times that of the original distribution. If one divides the two standard deviation values by $\sqrt{2}$ in order to estimate the measurement precision of the instrument in each channel, we obtain $1.16 \pm 0^\circ\!.13$ in the position angle and 1.92 ± 0.22 mas in separation. Since we have combined the astrometric results of both channels in Table 2, this would result in a further decrease in these numbers by another factor of $\sqrt{2}$, so that the final expected intrinsic precision is $0.82 \pm 0^\circ.10$ in the position angle and 1.36 ± 0.16 mas in separation. Of course, this does not include contributions to the error from the scale calibration, both random and systematic. Further work on the scale is clearly needed and it is possible that the values in Table 2 could be slightly revised when better calibrations are available, but at this point the numbers are consistent with those obtained over a long period of time with the RYTSI speckle camera and detailed in Horch et al. (2008).

The second method used to characterize the astrometry was to compare our measures for objects in Table 2 with orbital ephemeris predictions in cases where high-quality orbits exist. There are five such objects in Table 2, and these are listed in Table 3 together with references for the orbital elements used in our calculations of the ephemeris positions. All five objects have uncertainties available for their orbital elements, and these have been used to estimate uncertainties in the predicted position for the epochs of observation here. The residuals in the position angle and separation when comparing to positions obtained from the individual channels of the instrument are plotted in Figure 7. Also, the average residuals for each object using the last five measures in the *Fourth Catalog of Interferometric Measures*

Table 2
Double Star Speckle Measures

WDS (α,δ J2000.0)	HR, ADS DM, or HD	Discoverer Designation	HIP	Date (2000+)	θ (°)	ρ (″)	Δm 447 nm	Δm 562 nm	Δm 692 nm
00085+3456	BD+34 3	HDS 17	689	2008.6910	111.0	0.084	···	0.52	0.43
				2008.6937	110.7	0.085	0.48	···	0.38
00121+5337	ADS 148	BU 1026Aa-B	981	2008.6967	310.9	0.332	1.91	···	1.32
00179+3435	BD+33 24	HDS 41	1441	2008.6910	283.0	0.514	···	3.02	2.69
				2008.6937	283.2	0.520	3.43	···	2.63
00258+1025	BD+09 41	HDS 57	2035	2008.6937	95.0	0.113	···	···	0.94[a]
00261−1123	BD−12 63	YR 4	2066	2008.6938	189.8	0.401	···	···	3.11
00277−1625	ADS 366	YR 1Aa,Ab	2190	2008.6938	129.3	0.068	···	···	0.52[a]
00284−2020	HR 108	B 1909	2237	2008.6938	294.5	0.192	0.97	···	0.92
00321−1218	BD−13 89	HDS 71	2532	2008.6938	320.8	0.308	···	···	0.77
00469+4339	BD+42 170	HDS 102	3669	2008.6911	102.1	0.135	···	1.51	1.27
00495+4404	BD+43 159	HDS 109	3857	2008.6911	327.6	0.082	···	2.39	2.03
00512+1405	BD+13 115	YSC 18	3983	2008.6967	234.8	0.148	···	···	2.06
00516+4412	BD+43 165	YR 19	···	2008.6911	126.6	0.102	···	0.94	0.92
00541+6626	BD+65 106	YSC 19Aa	4239	2008.6911	124.1	0.070	···	0.93	0.72
00541+6626	BD+65 106	HDS 117AB	4239	2008.6911	110.1	0.903	···	···	3.71
01038+5212	BD+51 219	COU2257	4976	2008.6911	80.4	0.425	···	0.63	0.46
01108+6747	BD+67 98	HDS 155	5531	2008.6911	198.7	0.084	···	0.96	0.89
01129+5136	BD+50 238	HDS 160	5674	2008.6911	69.0	0.144	···	2.04	1.89
01284+0758	BD+07 214	YR 7Ba	6873	2008.6912	45.0	0.463	···	3.28	3.01
01297+2250	ADS 1183	A 1910AB	6966	2008.6912	188.1	0.170	···	0.68	0.60
02128−0224	ADS 1703	TOK 39Aa,Ab	10305	2008.6912	158.2	0.025	···	0.79	0.84[a]
02164+0437	BD+03 313	YR 8	10596	2008.6912	348.2	0.038	···	1.20	0.90
02167+0632	BD+05 309	YSC 20	10616	2008.6912	334.2	0.103	···	···	2.41
02366+1227	HR 763	MCA 7	12153	2008.6968	130.2	0.066	0.36	···	0.26
02449+1007	BD+09 359	TOK 1Aa	12828	2008.6968	187.7	0.098	···	···	3.43
02584+1914	BD+18 382	YR 9	13855	2008.6913	241.8	0.608	···	3.88	3.44
03125+1857	BD+18 430	HDS 408	14929	2008.6914	355.0	0.094	···	0.42	0.42
03151+1618	ADS 2429	HU 1055AB	15134	2008.6914	120.7	0.435	···	1.04	0.91
03208+2311	BD+22 475	OCC 771	15586	2008.6914	63.4	0.600	···	4.31	3.77
03209+2031	BD+19 511	HDS 418	15597	2008.6914	340.5	0.585	···	4.21	4.53
03213+1038	BD+10 432	HEI 449	15633	2008.6968	63.6	0.218	0.52	···	0.62
03228+2045	BD+20 551	HDS 423	15737	2008.6914	293.5	0.375	···	3.48	3.79
03272+0944	HR 1038	HDS 433	16083	2008.6968	124.8	0.191	4.19	···	3.20
03385+1336	BD+13 576	YR 10	16991	2008.6968	80.2	0.309	···	···	3.29
03496−0220	BD−02 726	YR 23	17895	2008.6969	328.9	0.310	1.52	···	0.90
03596+0436	BD+04 614	YSC 21	18650	2008.6969	295.8	0.188	···	···	3.48
04047+1731	BD+17 676	YSC 22	19036	2008.6914	91.3	0.348	···	2.84	3.04
04073+1332	BD+13 646	YSC 23	19229	2008.6914	333.4	0.145	···	2.84	2.60
04099+1552	BD+15 590	YSC 24	19451	2008.6914	285.0	0.565	···	2.15	2.19
04102+1722	BD+16 564	HEI 35	19472	2008.6915	335.6	0.428	···	1.56	1.26
04116+2950	BD+29 676	YR 11	19572	2008.6969	87.6	0.494	···	···	3.57
04136+0743	ADS 3064	A 1938	19719	2008.6969	295.5	0.117	1.06	···	0.91
04184+1725	HD 285663	AT 4	20086	2008.6915	251.6	0.686	···	···	3.40
04196+2104	HD 27310	HDS 553	20181	2008.6969	20.8	0.818	···	···	3.51
04242+1445	BD+14 693	HDS 564	20553	2008.6915	239.2	0.370	···	3.07	2.64
04256+1556	HR 1391	FIN 342Aa	20661	2008.6970	173.0	0.084	0.37	···	0.34
04258+1800	HD 27990	COU2682	20679	2008.6915	326.4	0.290	···	1.34	1.12
04297+1211	BD+11 618	HDS 578	20960	2008.6970	245.8	0.285	···	···	2.97
18154+5720	BD+57 1856	HDS2577	89455	2008.6932	100.8	0.277	···	···	0.77
20375+1436	ADS 14073	BU 151AB	101769	2008.6909	14.1	0.448	···	1.27	1.33
20396+1555	ADS 14121	WCK 2Aa	101958	2008.6909	211.6	0.216	···	2.66	2.41
23209+1643	BD+15 4809	HEI 88	115279	2008.6909	158.2	0.175	···	1.11	0.92
23271+1307	BD+12 4986	HDS3339	115751	2008.6910	237.7	0.422	···	3.03	2.98

Note. [a] Quadrant ambiguous.

of Binary Stars (Hartkopf et al. 2001) are plotted. The data show that the DSSI measures are generally in agreement with the orbit predictions, to within the precision that can be stated given uncertainties of the orbital elements in hand. The sign of the DSSI residual, either positive or negative, also usually agrees with the average residual of the last five Fourth Catalog observations. The only significant departure from this is with the middle point of the separation residuals, WCK 2Aa, but the most recent two observations in the Fourth Catalogue have negative residuals, in agreement with the DSSI result. We conclude that

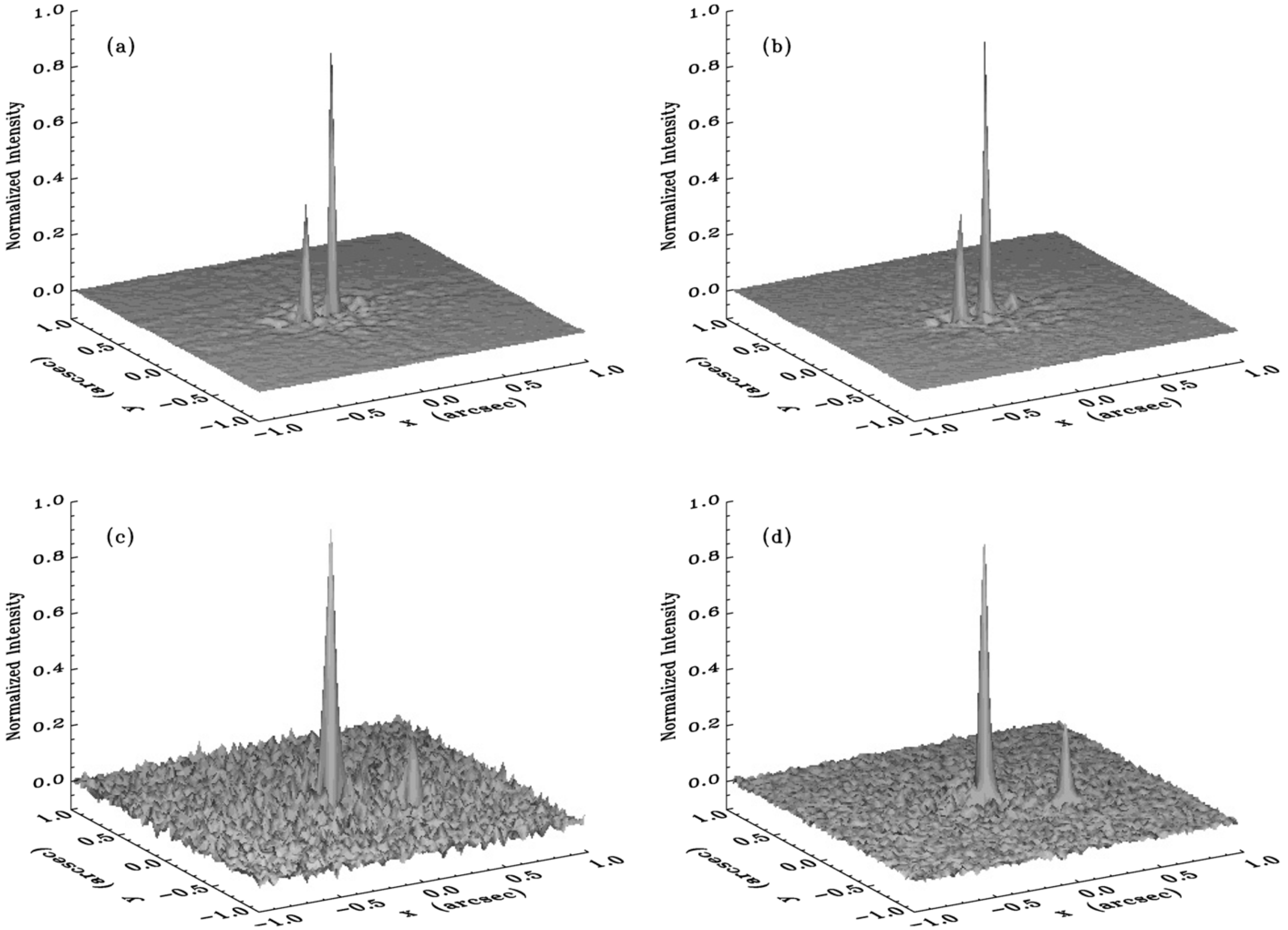

Figure 5. Sample reconstructed images. (a) A 1910AB = HIP 6966 at 562 nm. (b) A 1910AB = HIP 6966 at 692 nm. (c) HEI 35 = HIP 19472 at 562 nm. (d) HEI 35 = HIP 19472 at 692 nm. In all plots, North is in the positive x-direction and East is in the positive y-direction.

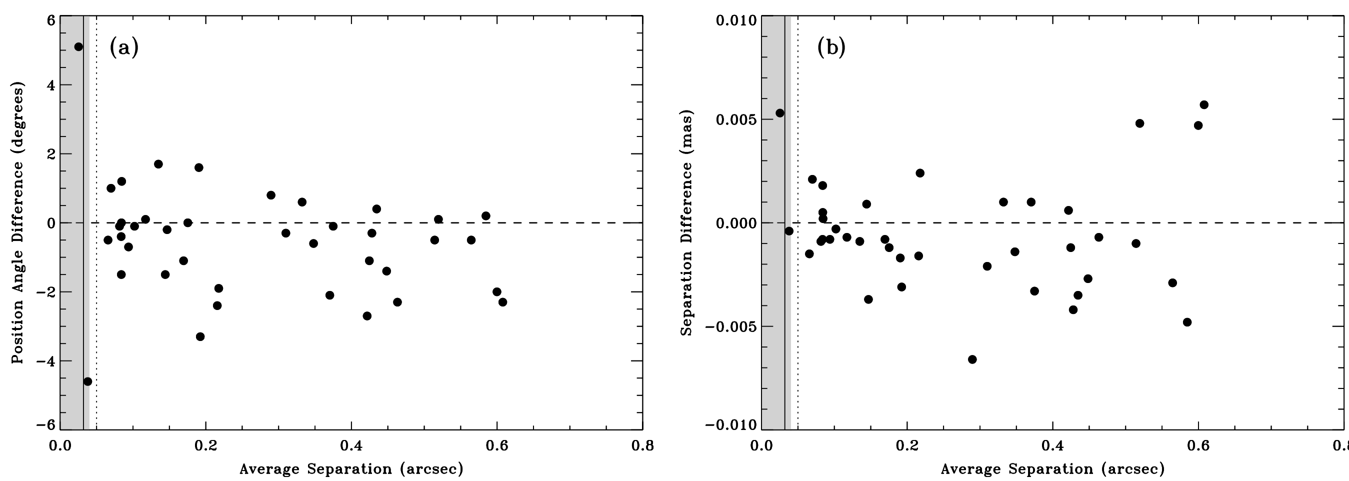

Figure 6. (a) Differences in the position angle obtained in the two channels as a function of average separation. (b) Differences in separation obtained in the two channels as a function of average separation. In both plots, the diffraction limit for each filter is marked at the left: the solid line for 447 nm, the shaded region for 562 nm, and the dotted line for 692 nm.

the scale determination for the measures in Table 2 is consistent with previous speckle measures made with other instruments.

4.2. Photometric Precision

We also seek to characterize the photometric precision of the measures in Table 2. To do so, we follow the method in Horch et al. (2004), where seeing times separation is used to estimate the decorrelation of the secondary star's speckle pattern relative to that of the primary. In that work, the authors chose not to report a magnitude difference if the seeing times separation was above 0.6 arcsec squared. As those data were taken at the WIYN Telescope with a similar speckle camera, we expect that the cutoff value will remain approximately the same. In the

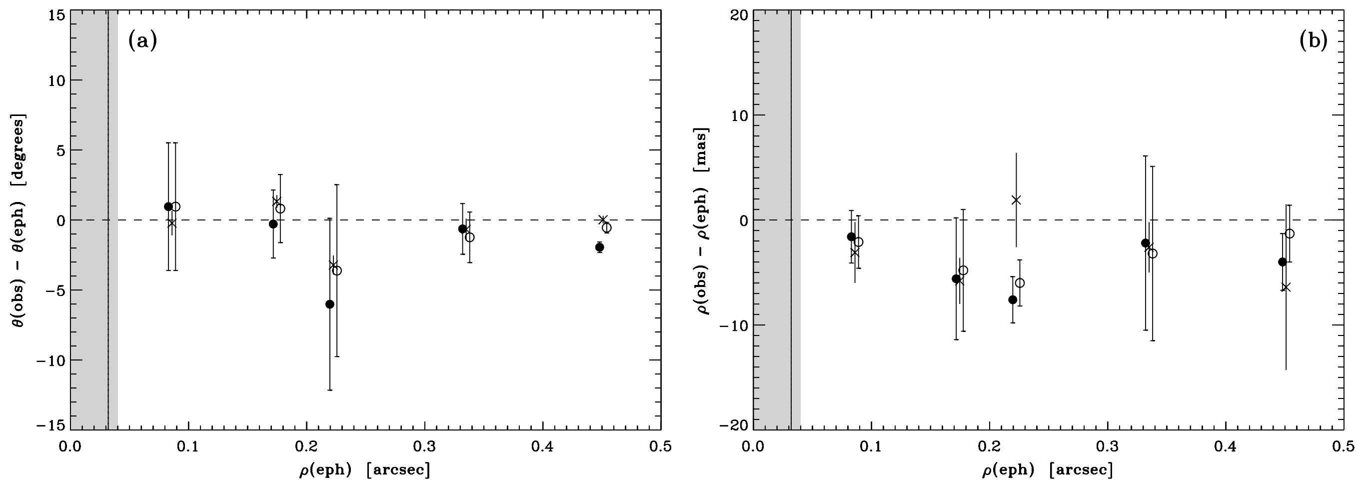

Figure 7. (a) Position angle residuals when comparing to high-quality orbits discussed in the text. (b) Separation residuals when comparing to the high-quality orbits discussed in the text. In both plots, the diffraction limit is marked as in Figure 5 for each wavelength; open circles represent data from the transmissive channel, filled circles represent data from the reflective channel, and crosses represent the average residual using the last five measures appearing in the *Fourth Interferometric Catalog*. The error bars in the vertical direction represent the uncertainty based on the published uncertainties of the orbital elements for the DSSI residuals, and the standard error of the five residuals for the *Fourth Catalog* data.

Table 3
Orbits Used for the Measurement Precision Study

Discoverer Designation	HIP	WDS	Grade	Reference
BU 1026AB	981	00121+5337	2	Hartkopf et al. 1996
A 1910AB	6966	01297+2250	2	Hartkopf et al. 1996
FIN 342Aa	20661	04256+1556	1	McAlister et al. 1988
BU 151AB	101769	20375+1436	1	W. I. Hartkopf 2001, private communication
WCK 2Aa,Ab	101958	20396+1555	2	Söderhjelm 1999

case of the data presented in this paper, all observations had seeing times separation below the cutoff value, indicating that speckle decorrelation should not be a significant factor in the photometric results in Table 2.

The DSSI data can therefore be compared with the magnitude difference result in the *Hipparcos* Catalogue (ESA 1997) for all objects where it exists. This is shown in Figure 8(a). The DSSI data are clearly strongly correlated with the *Hipparcos* results, though there are systematic differences from filter to filter, as expected. The magnitude differences appearing in the *Hipparcos* Catalogue are in the H_p filter, which is a broad filter slightly bluer than *V*. The closest match to this among the three DSSI filters is the 562 nm filter, though even this is not perfect. Nonetheless, we show a residual plot comparing the 562 nm result to ΔH_p in Figure 8(b). Systems where the primary is most likely a giant (as judged from the system Hertzsprung–Russell diagram (H–R diagram) position) have been removed. The average residual is 0.23 ± 0.05 mag for all 14 points in the plot. However, some of the systems have very large uncertainties in ΔH_p. If only those with $\delta(\Delta H_p) < 0.15$ mag are considered (leaving seven systems), then the average residual is reduced somewhat to 0.18 ± 0.05.

For the seven systems with $\delta(\Delta H_p) < 0.15$, the standard deviation of the residuals is 0.11 ± 0.03 and the average value of $\delta(\Delta H_p)$ is 0.08. We assume that the errors from the *Hipparcos* measures and those presented here add in quadrature so that

$$\delta(\Delta m_{562} - \Delta H_p) = \sqrt{\delta(\Delta H_p)^2 + \delta(\Delta m_{562})^2}. \quad (4)$$

This then implies that $\sqrt{0.08^2 + \delta(\Delta m_{562})^2} = 0.11$ or that $\delta(\Delta m_{562}) \approx 0.08$. This number is comparable to the minimum value obtained as a function of the magnitude difference in Horch et al. (2008) for the RYTSI camera.

We can also compare the photometric measures here with those of the RYTSI camera directly. In that case, there are two pairs of filters very close in central wavelength: the 562 nm DSSI filter can be compared with the results using the 550 nm RYTSI filter and the 692 nm DSSI filter can be compared with the 698 nm RYTSI filter. After identifying the objects in Table 2 that have RYTSI observations in the relevant filters, the RYTSI magnitude differences were averaged in cases where more than one observation existed, and the difference between the DSSI result and the RYTSI result was calculated. These are plotted in Figure 9. The error bars in the plot are the standard errors of the RYTSI observations.

In the case of the 562–550 nm comparison, there are 10 objects represented in the plot. The mean residual is 0.16 ± 0.05 mag, though several objects again have large uncertainties. If one applies the same cut in $\delta(\Delta m_{550})$ as was performed for the *Hipparcos* data, namely $\delta(\Delta m_{550}) < 0.15$ mag, then five systems remain with average $\delta(\Delta m_{550}) = 0.05$ mag. The standard deviation of the differences of these five measures is 0.14 mag. Assuming as above that the errors from the two cameras add in quadrature to arrive at 0.14, then this implies that the DSSI measures have an approximate precision of 0.13 mag

Finally for the 692–698 nm comparison, the mean residual is 0.01 ± 0.06 mag for the 13 systems with RYTSI data. If one again applies the cut of $\delta(\Delta m_{698}) < 0.15$, this leaves eight systems with standard deviation of 0.26 mag and average $\delta(\Delta m_{698}) = 0.04$. Therefore, using the same reasoning as in the previous two comparisons, we would deduce an uncertainty in DSSI measures of 0.25 mag.

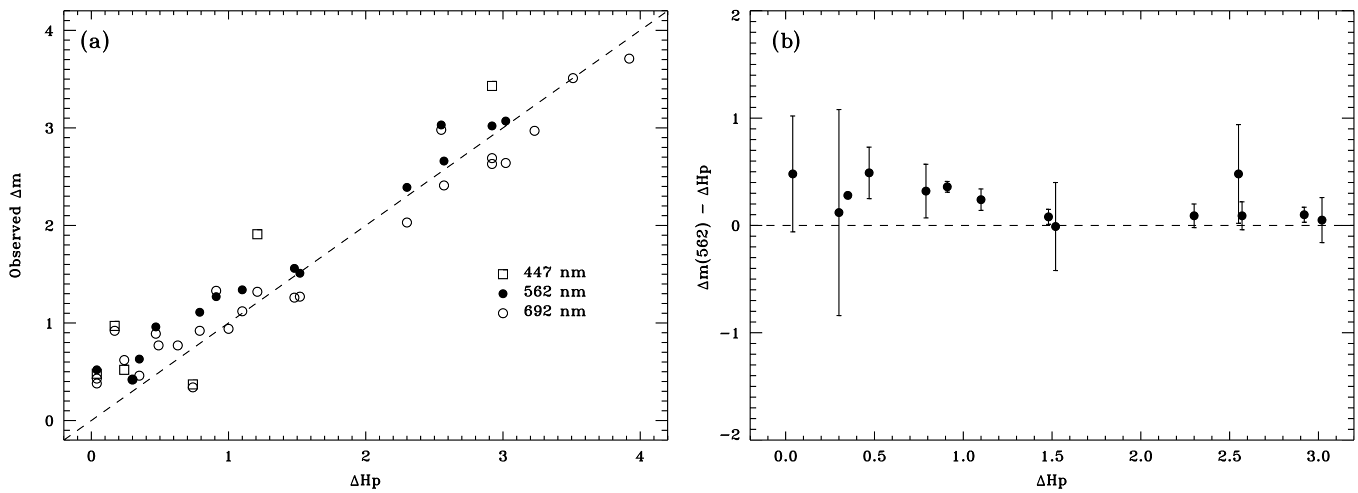

Figure 8. (a) Observed magnitude difference versus ΔH_p for observations appearing in Table 2. The dashed line marks the line $y = x$. (b) The difference between magnitude difference measures taken in the 562 nm filter and the value ΔH_p appearing in the *Hipparcos* Catalogue. The vertical error bars in this case are the uncertainties in ΔH_p.

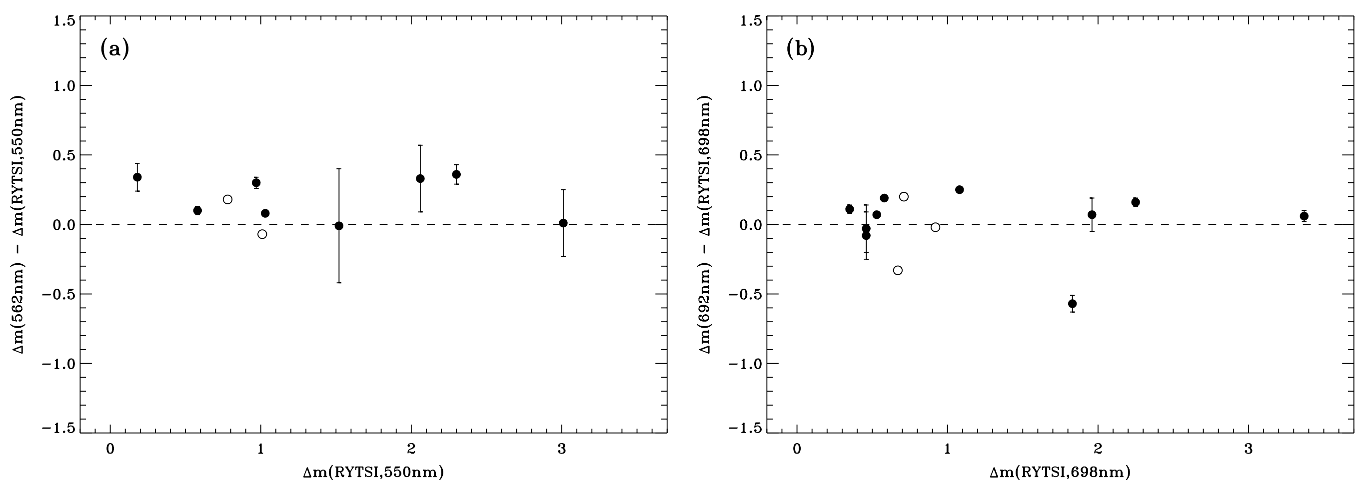

Figure 9. (a) Differences in magnitude difference between measures in Table 2 at 562 nm and previous measures using the RYTSI speckle camera at 550 nm. (b) Differences in magnitude difference between measures in Table 2 at 692 nm and previous measures using the RYTSI speckle camera at 698 nm. In both plots, the vertical error bars are the standard errors of the RYTSI measures, if more than one exists. Open circles indicate systems with only one RYTSI measure.

The average of the three comparisons gives a rough precision for DSSI measures of 0.15 ± 0.05 mag, which is again comparable to the photometric precision in Horch et al. (2008). There may be a small offset in the photometry obtained with DSSI relative to *Hipparcos* measures and RYTSI measures at 550 nm, as judged by the mean residual in these comparisons, and further work will be needed to characterize this. One way to approach this would be to obtain a calcite crystal that could be mounted inside the DSSI camera in front of the tip-tilt mirrors on future runs. Since the relative intensity of the ordinary and extraordinary rays through the crystal is a known function of crystal orientation, a photometric calibration could be obtained by observing point sources. Each observation would effectively yield double speckles and could be analyzed as a binary star. The observed curve of magnitude difference as a function of the orientation angle of the crystal could then be compared with the theoretical prediction. While calibration of the photometry may be needed, the intrinsic precision of the measures here appears to be sufficiently high to support the statement that the DSSI is capable of delivering magnitude differences and component colors for many binaries in a survey capacity in the future.

4.3. Subdiffraction-Limited Results

Two of the objects listed in Table 2, namely TOK 39Aa,Ab and YR 8, were found to be below the diffraction limit in both filters used in our DSSI observation. In the past, separations below the diffraction limit have not generally been published by speckle observers. This situation results in blended, elongated speckles due to the presence of the close companion, and it has not been possible to rule out residual atmospheric dispersion or other systematic effects as the cause of the elongated shape of the speckles, let alone to measure that elongation reliably. However, as explained in Horch et al. (2006), if dispersion were the explanation of the observed power spectrum, the "separation" observed would be a function of wavelength and would therefore be very different in the two filters of a DSSI observation. In addition, the deduced position angle would be along a line from the object to the zenith. The ability of the DSSI to observe in two colors simultaneously gives substantial leverage in distinguishing between binarity and dispersion.

An example of this is shown in Figure 10. Spatial frequency power spectra are shown for three objects, two of which have a separation that is above the diffraction limit (A 1910AB and HDS 17) and one where it is below (TOK 39Aa,Ab). Power spectra in both filters for each observation are shown, and the mirror image effect in the raw data has been removed. Taken together, the sequence illustrates what happens to the power spectrum as the separation of the two stars in a binary system is decreased: the fringes become more widely spaced. (The different position angles of the three objects give different orientations to the fringe patterns in each of the three cases, but that is not important for the discussion here.) In the Fourier domain, the diffraction limit is represented by a circle of a certain radius centered on the origin, beyond which no signal is obtained. (In these plots, the circle has diameter just slightly smaller than the side length of the arrays shown and the origin is at the center of each array.) When the separation is below the diffraction limit, only the central fringe is visible because the first-order fringes already lie outside the diffraction limit. Nonetheless, if the object is binary, a cosine-squared fit to the power spectrum will yield a separation, position angle, and magnitude difference just as with larger-separation objects, based on the shape of the central fringe alone. Dispersion can be ruled out as the cause of the central fringe if the separation obtained in both filters is very similar. While sub-diffraction-limited observations with the DSSI cannot be considered to have the precision of the measures obtained above the diffraction limit at this stage, we judge it to be very likely that the DSSI has successfully detected the binary nature of TOK 39Aa,Ab and the other object below the diffraction limit in Table 2, YR 8, based on the similarity of the power spectra in both filters.

With the measurement of smaller separations, smaller period systems become approachable and orbital elements can potentially be determined in a relatively short amount of time. For example, at the discovery epoch of YR 8, the system had a separation of approximately 0.1 arcsec, considerably higher than the current value of 0.038 arcsec, though the position angle has changed only by a modest amount. The separation and position angle of TOK 39Aa,Ab remain fairly similar to the values obtained by Tokovinin & Cantarutti (2008), though the position angle change is of course dependent on the sense of the rotation and would be either 43° or 317°, taking the two position angles at face value. (Due to the extremely small separation and modest magnitude difference, it is not possible to be definitive about the quadrant assignment for our observation.) If the value of 317° is used, this would imply an orbital period of approximately 1.25 years, assuming a circular orbit. Using the parallax found in the *Hipparcos* Catalogue of 21.71 ± 1.67 mas, and noting that the spectral type of the system is F8V (again from *Hipparcos*), the components may be roughly approximated by F8V and G1V, given the modest magnitude differences obtained in our observations. A mass sum of ∼2.2 solar masses is therefore probably appropriate for this system. These data would imply a semimajor axis of 33 mas, which is larger than the separations observed but certainly indicates that a subdiffraction-limited separation at a 3.5 m aperture is quite reasonable. Both YR 8 and TOK 39Aa,Ab are worthy of sustained future observations.

5. CONCLUSIONS

We have presented the first results obtained with the DSSI, a new speckle imaging system designed to take data in two colors simultaneously. The main body of results includes relative astrometry and photometry for 52 binary star systems and includes repeated observations on two systems for a total of 54 observations. The instrument design and the basic capabilities have been described. Astrometric precision below 2 mas per observation appears possible at the 3.5 m aperture, as does photometric precision of 0.15 mag per observation. With repeated observations, the latter allows for precise magnitude and color information to be determined for the components of binary systems in survey capacity. In future observations, careful calibration of the astrometry and photometry will be important in achieving the best possible results with the system, but the initial observations are overall quite promising.

The initial observations also included two objects below the diffraction limit of the telescope. Simultaneous observation in two filters provided the means with which to rule out dispersion as the cause of the broad fringe observed in the power spectrum and to deduce relative astrometry and photometry for these systems. Seven objects were resolved for the first time in observations presented here, with separations ranging from 0.070 to 0.565 arcsec.

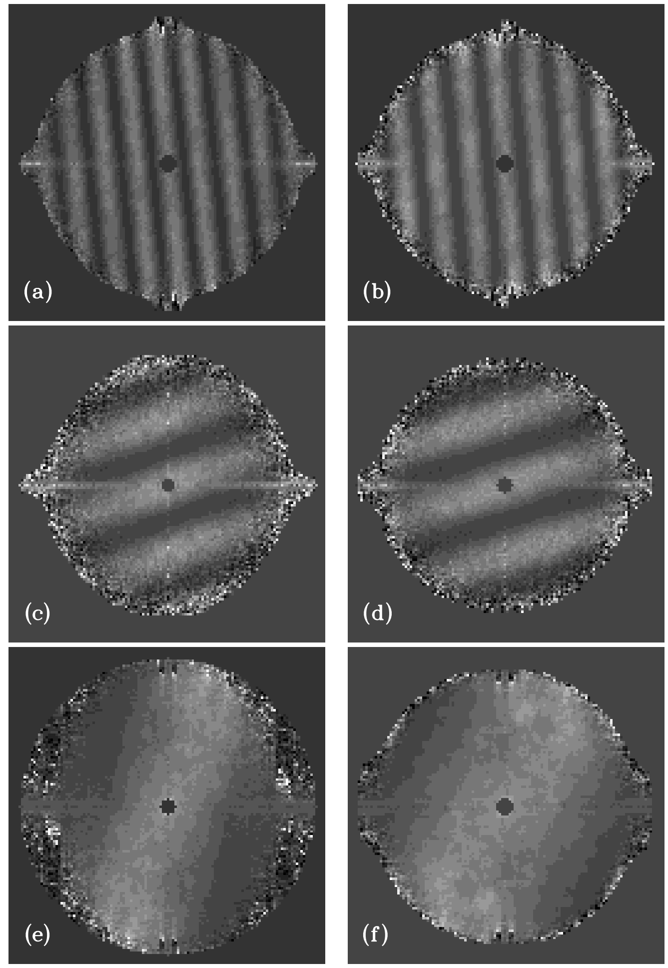

Figure 10. Power spectra for three observations with DSSI. A 1910AB = HIP 6966 at (a) 562 nm and (b) 692 nm. The separation is 0.170 arcsec. HDS 17 = HIP 689 at (c) 562 nm and (d) 692 nm. The separation is 0.084 arcsec. TOK 39Aa,Ab = HIP 10305 at (e) 562 nm and (f) 692 nm. The separation is 0.025 arcsec. With decreasing separation, there are fewer fringes in the power spectrum before the diffraction limit is reached. In the case of TOK 39Aa,Ab, only the central (zeroth order) fringe is seen in these plots because the diffraction limit is reached before higher order fringes are visible. This indicates that speckles on the image plane are not resolved but blended; nonetheless, the similarity in appearance between the two colors gives confidence that the signature is not due to residual dispersion.

We thank S. Howell, W. Sherry, K. Reetz, and C. Corson for their assistance at the telescope during the 2008 September run. We also thank the anonymous referee for his/her helpful comments. This work was funded by NSF Grants AST-0504010 and AST-0751361. It made use of the Washington Double Star Catalog maintained at the U.S. Naval Observatory and the SIMBAD database, operated at CDS, Strasbourg, France.

REFERENCES

Balega, I. I., Balega, Y. Y., Hofmann, K.-H., Maksimov, A. F., Pluzhnik, E. A., Schertl, D., Shkhagosheva, Z. U., & Weigelt, G. 2002, A&A, 385, 87
Balega, I. I., Balega, Y. Y., Hofmann, K.-H., Malogolovets, E. V., Schertl, D., Shkhagosheva, Z. U., & Weigelt, G. 2006, A&A, 466, 649
Balega, I. I., Balega, Y. Y., Hofmann, K.-H., Pluzhnik, E. A., Schertl, D., Shkhagosheva, Z. U., & Weigelt, G. 2005, A&A, 433, 591
ESA 1997, The Hipparcos and Tycho Catalogues, ESA SP 1200
Hartkopf, W. I., Mason, B. D., & McAlister, H. A. 1996, AJ, 111, 370
Hartkopf, W. I., McAlister, H. A., & Mason, B. D. 2001, AJ, 122, 3480 (See also http://ad.usno.navy.mil/wds/int4.html)
Hoffleit, E. D., & Jaschek, C. 1982, The Bright Star Catalogue (New Haven: Yale Univ. Observatory)
Horch, E. P., Franz, O. G., & van Altena, W. F. 2006, AJ, 132, 2478
Horch, E. P., Meyer, R. D., & van Altena, W. F. 2004, AJ, 127, 1727
Horch, E. P., van Altena, W. F., Cyr, W. M., Kinsman-Smith, L., Srivastava, A., & Zhou, J. 2008, AJ, 136, 312
Johnson, H. L. 1965, ApJ, 141, 923
Lohmann, A. W., Weigelt, G., & Wirnitzer, B. 1983, Appl. Opt., 22, 4028
McAlister, H. A., Hartkopf, W. I., Bagnuolo, W. G., Jr., Sowell, J. R., Franz, O. G., & Evans, D. S. 1988, AJ, 96, 1431
Mermilliod, J.-C., Mermilliod, M., & Hauck, B 1997, A&AS, 124, 349
Meyer, R. D., Horch, E. P., Ninkov, Z., van Altena, W. F., & Rothkopf, C. A. 2006, PASP, 118, 162
Pickles, A. J. 1998, PASP, 110, 749
Scardia, M., Prieur, J.-L., Pansecchi, L., Argyle, R. W., Sala, M., Ghigo, M., Koechlin, L., & Aristidi, E. 2006, A&A, 367, 1170
Scardia, M., Prieur, J.-L., Sala, M., Ghigo, M., Koechlin, L., Aristidi, E., & Mazzoleni, F. 2005, A&A, 357, 1255
Scardia, M., et al. 2007, A&A, 374, 965
Schmidt-Kaler, T. 1982, in Landolt-Börnstein New Series, Group 6, Vol. 2b, Stars and Star Clusters, ed. K. Schaefers & H.-H. Voigt (Berlin: Springer), 1
Söderhjelm, S. 1999, A&A, 341, 121
Tamazian, V. S., Docobo, J. A., Balega, Y. Y., Melikian, N. D., Maximov, A. F., & Malogolovets, E. V. 2008, AJ, 136, 974
Tokovinin, A., & Cantarutti, R. 2008, PASP, 120, 170
Tyler, D. W., Muralimanohar, H., & Borelli, K. J. 2007, PASP, 119, 183